BIOPHYSICS

Atomic-scale characterization of mature HIV-1 capsid stabilization by inositol hexakisphosphate (IP6)

Alvin Yu[1], Elizabeth M. Y. Lee[2], Jaehyeok Jin[1], Gregory A. Voth[1]*

Inositol hexakisphosphates (IP6) are cellular cofactors that promote the assembly of mature capsids of HIV. These negatively charged molecules coordinate an electropositive ring of arginines at the center of pores distributed throughout the capsid surface. Kinetic studies indicate that the binding of IP6 increases the stable lifetimes of the capsid by several orders of magnitude from minutes to hours. Using all-atom molecular dynamics simulations, we uncover the mechanisms that underlie the unusually high stability of mature capsids in complex with IP6. We find that capsid hexamers and pentamers have differential binding modes for IP6. Ligand density calculations show three sites of interaction with IP6 including at a known capsid inhibitor binding pocket. Free energy calculations demonstrate that IP6 preferentially stabilizes pentamers over hexamers to enhance fullerene modes of assembly. These results elucidate the molecular role of IP6 in stabilizing and assembling the retroviral capsid.

INTRODUCTION

The capsids of HIV-1 encase and protect the retroviral genome from natural host defense mechanisms but are transiently stable complexes. These capsids are assembled inside viral particles after proteolytic cleavage of the Gag polyprotein in a large-scale morphological transition of the virus termed maturation (*1*) and must be disassembled before integration of the virus' genetic information into the host cell (*2*). Structurally, immature Gag lattice precursors form incomplete spherical assemblies, composed primarily of hexamers of uncleaved Gag polyprotein (*3*), while mature HIV-1 capsids are fullerene-like structures, composed of hexamer and pentamer building blocks of a single capsid domain (CA) protein (*4*). There are exactly 12 pentamers in a mature capsid that is topologically required to enclose the shell and impart curvature onto the CA lattice. Biochemical reconstitutions of CA assemblies show that CA can self-assemble into a wide range of morphologies, including helical tubes and fullerene cones (*5*). CA lattices composed solely of hexamers, however, form helical tubes rather than fullerene structures.

Characterization of capsids with fullerene geometries (*6*) that resemble those imaged by electron cryo-tomography within intact virions has been notoriously difficult, in part because of the short lifetimes under which capsids remain stable in isolation and the structural heterogeneity of the capsids themselves. Recent x-ray crystal structures demonstrate that pH-gated pores found at the center of hexamer subunits are distributed throughout the capsid surface and contain an electropositive ring of arginines (R18) at the narrowest region of the pore (*7*, *8*). Polyanions, including nucleotides, readily bind to the arginine ring. In particular, inositol hexakisphosphate (IP6) is a cellular polyanion that is abundantly present in the cytosol and enriched in packaged viral particles that bud off from the cell (*9*). The addition of IP6 to in vitro reconstitutions of the capsid drastically increases the stable lifetimes of the HIV-1 capsid from several minutes to over 10 hours and promotes the assembly of fullerene capsids (*9*, *10*). Viruses that fail to package IP6 do not

mature properly and have unstable capsids (*11*). Previous molecular simulations examined the conformational fluctuations of portions of the immature Gag lattice in the presence and absence of an IP6 ligand and found noticeable distortions of the six-helix bundle in the Gag spacer peptide 1 without IP6 (*10*). Mutagenesis studies have revealed that removal of electrostatic repulsion between CA domains at the arginine ring (R18A) causes assembly behavior consistent with an increased frequency of pentamer incorporation (*5*, *12*). Despite these advances, there are no studies on whether IP6 interacts with pentamers, and the molecular mechanisms that underlie the increased stability and enhanced assembly of the mature capsid by IP6 remain unclear.

To investigate this, we performed long time scale all-atom (AA) molecular dynamics (MD) simulations of CA proteins with IP6 in bulk solution and analyzed the mechanisms by which IP6 binds to capsid pores. This analysis reveals that CA hexamers and pentamers have unexpectedly different binding modes for IP6, despite the high structural similarity between the capsid oligomers. To identify the protein-ligand interactions made during the IP6 binding process, we calculated three-dimensional (3D) density maps for IP6 that specify the regions the ligand occupies during dynamical simulation. These density maps show two weaker-affinity sites for IP6 and CA, one of which corresponds to a previously discovered capsid inhibitor binding pocket. Free energy calculations of the binding process indicate that IP6 stabilizes pentameric CA states to a greater extent than hexameric CA states. These results suggest that IP6 binding shifts assembly conditions toward an increased population of pentamers to stabilize the fullerene capsid.

RESULTS

CA hexamers and pentamers have differential IP6 binding modes

MD simulations of the complete mature HIV-1 capsid (~100 million atoms, Fig. 1A) (*13*) are computationally costly. Instead, to investigate how IP6 stabilizes the capsid, we simulated individual hexamer and pentamer components of the capsid [Protein Data Bank (PDB) ID: 3H47, 5HGL, and 5MCY] using unbiased, microsecond time scale AA MD simulations on the special-purpose computer hardware, Anton 2, at the Pittsburgh Supercomputing Center (*14*). Similar to

[1]Department of Chemistry, Chicago Center for Theoretical Chemistry, Institute for Biophysical Dynamics, and James Franck Institute, The University of Chicago, Chicago, IL 60637, USA. [2]Pritzker School of Molecular Engineering, The University of Chicago, Chicago, IL 60637, USA.
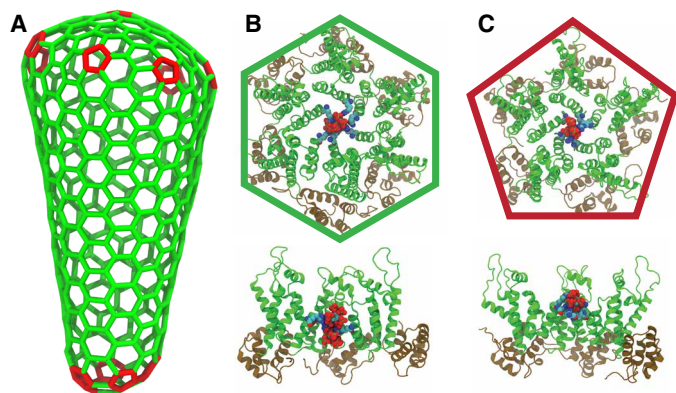*Corresponding author. Email: gavoth@uchicago.edu

Fig. 1. IP$_6$ binds to the CA hexamer and pentamer. (**A**) The fullerene structure of HIV capsids contains exactly 12 pentameric defects. The geometry for the HIV-1 capsid was derived from cryo–electron tomography images of intact virions (*6*). Pentameric defects are colored red. (**B**) Two IP$_6$ molecules bind to the R18 ring in the central pore of the CA hexamer (PDB ID: 5HGL) after 0.73 μs of AA MD simulations. The bound complex is shown in a top-down and side view. (**C**) A single IP$_6$ molecule binds to the R18 ring at a pore in the CA pentamer (PDB ID: 5MCY) after 1.98 μs of AA MD simulations. The bound complex is shown in a top-down and side view. In the MD simulations for (B) and (C), IP$_6$ molecules were initially placed in bulk solvent, ~10 Å away from the CA domains. The NTD of CA is colored in green, and the CTD of CA is colored in brown. R18 residues are shown in cyan.

prior studies, IP$_6$ was initially added to the bulk solvent, approximately 10 Å away from any nonwater molecules (*15*, *16*). Four systems each for the CA hexamer and pentamer were prepared with IP$_6$ in randomized positions in bulk solvent and selected for longer time scale simulations on Anton 2 (see Materials and Methods for a complete description). In aggregate, the AA MD simulations totaled 32 μs for the hexamer and pentamer systems. In all cases, IP$_6$ was found to bind to the pore of the capsomere.

After exhaustive MD simulation (~4 μs per trajectory) of the CA hexamers, two IP$_6$ molecules bind to a central arginine (R18) ring that lines the hexameric pore. A single IP$_6$ ligand occupies the volume ~3 Å above the R18 ring, with phosphate groups coordinated by the functional groups of the R18 side chains, whereas a second IP$_6$ molecule binds below the arginine ring, also coordinated by the R18 guanidino groups, proximal to the CA C-terminal domain (CTD) (Fig. 1B and fig. S1). These binding poses for IP$_6$ are consistent with x-ray crystal structures of the mature CA hexamer in complex with IP$_6$, which reveal electron densities for positions above and below the R18 ring (*9*, *10*). Once bound, IP$_6$ did not unbind from the R18 ring in the course of our simulations.

To our surprise, for all pentamer trajectories, only a single IP$_6$ molecule bound to the R18 ring (Fig. 1C and fig. S1). The closely packed positive charges of the R18 ring are mitigated by contacts with negatively charged phosphate groups on IP$_6$. IP$_6$ binds above the ring and does not interact notably with protein residues below the R18 ring. Despite the overall structural similarities between capsomeres of the capsid shell, our simulations indicate that IP$_6$ associates with hexamers and pentamers using distinctly different binding modes.

Molecular mechanism of IP$_6$ binding to CA hexamers and pentamers

The binding of IP$_6$ not only enables the in vitro assembly of fullerene capsids from concentrated CA solutions ([CA] > 1 mM) but also markedly increases the lifetime of mature retroviral capsids synthe-

sized in the laboratory from minutes to hours (*17*). In the simulations, IP$_6$ exits bulk solvent and can enter the constricted pore from either the N-terminal domain (NTD) or CTD regions of the CA pentamer or hexamer. Snapshots of the binding process taken at various stages of ligand association are shown in Figs. 2 and 3, and the full process is shown in movies S1 and S2.

For the CA pentamer, IP$_6$ initially diffuses past the β-hairpin loop in the NTD. The side chains of the R18 ring are typically modeled to be planar in x-ray crystal structures and cryo–electron microscopy (cryo-EM) maps with torsional angles of $\chi_1 = -74°$, $\chi_2 = -156°$, $\chi_3 = 71°$, and $\chi_4 = 84°$ (Fig. 2, A and B), yet before binding, the pentameric complex shifts asymmetrically, involving a vertical separation of ~8 Å between the Cα carbons of R18 on helix H1 of the α and β domain, and the CA domains twist helically upward with $\beta < \gamma < \delta < \varepsilon < \alpha$ along the axis of the pore (Fig. 2, B and C). The pore arginine of the α-CA domain flips away from the plane with rotations about the R18 side chains ($\chi_1 = -70°$, $\chi_2 = 57°$, $\chi_3 = 60°$, and $\chi_4 = -179°$), likely reflecting unfavorable electrostatic interactions between the guanidino groups (Fig. 2C). The arginine side chain coordinates a phosphate group on IP$_6$ (Fig. 2D), as IP$_6$ binds to the pocket above the R18 ring. Additional arginine groups from the remaining CA domains contact the uncoordinated phosphate groups of the ligand, as IP$_6$ binds into the central pore, and the R18 ring relaxes to a planar configuration (Fig. 2, E to H).

In the CA hexamer, the overall complex does not twist asymmetrically, and IP$_6$ enters the pore initially from the CTD (Fig. 3, A to C). Salt-bridge interactions between K25 and E29 at the base of helix H1 break, and the lysine side chains interact with IP$_6$ (Fig. 3C). One of the pore arginines of the β-CA domain rotates downward to contact a phosphate group on IP$_6$ and forms a metastable complex between the protein and ligand, in which two IP$_6$ phosphate groups are coordinated at both ends by R18 and K25 (Fig. 3, D and E). A second IP$_6$ molecule enters the pore from the NTD region, anchored by an uncoordinated arginine in the R18 ring (Fig. 3F). Last, interactions between the first IP$_6$ molecule and K25 break, as both IP$_6$ ligands relax into the central binding sites above and below the R18 ring (Fig. 3, G and H). Previous simulations have also reported the presence of a salt-bridge contact between K30 and E28 that may stabilize CA pentamers more than hexamers (*18*). Our simulations were consistent with these results with closer contacts between K30 and E28 in the pentamer than hexamer trajectories (average Cα-Cα separation distances, 12.1 and 14.6 Å, respectively).

Four different initial conditions for the hexamers and pentamers were simulated, including combinations of open and closed CA conformations, containing protonated and deprotonated H12 residues (see table S1). X-ray structures had shown an iris-like opening of the hexamer pore in response to acidic pH conditions, hypothesized to occur by protonation of a critical histidine residue (H12), and a conformational change in the β-hairpin that gates the pore (*7*). In the simulations, however, IP$_6$ bound in the same fashion and made similar molecular interaction during binding to the R18 ring for CA complexes containing both protonated and deprotonated H12 and either open or closed conformations. In general, IP$_6$ bound more quickly to CA domains in open rather than closed conformations, and with protonated H12 residues rather than deprotonated H12 residues. The β-hairpin regions were quite flexible, suggesting that opening or closing of the proposed gate is driven more by small changes in the conformational ensembles adopted by the β-hairpin rather than by abrupt structural changes. IP$_6$ binding to pentamers
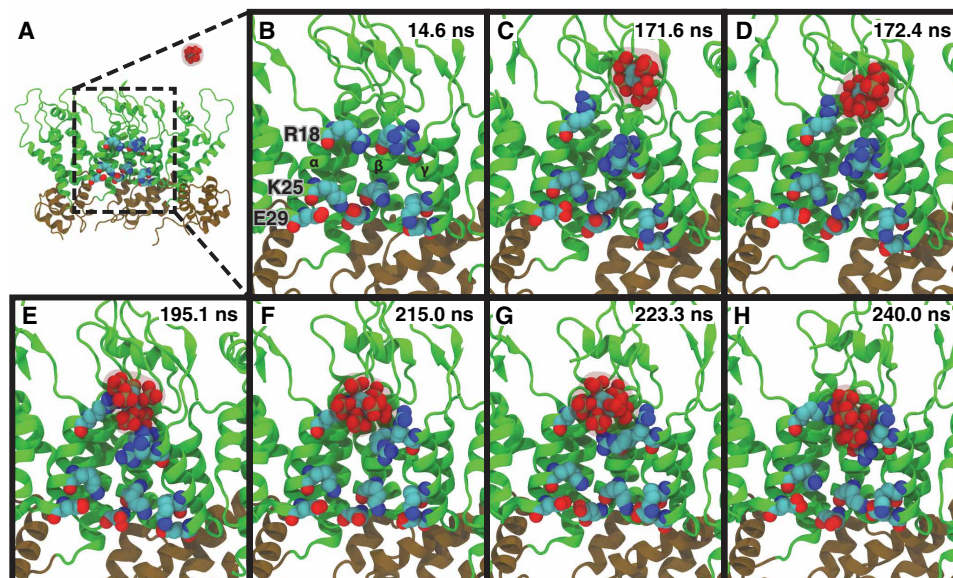
Fig. 2. Mechanism of IP$_6$ binding to CA pentamers. A series of snapshots from part of an MD trajectory show the chemical interactions involved in IP$_6$ binding to the CA pentamer. Three CA domains are shown in a side view of the pentamer, with helix H1 of the CA domain labeled as α, β, and γ, respectively. Two additional CA domains (δ and ε) are not shown for clarity. The R18 ring and residues (K25-E29) that form a salt-bridge interaction proximal to the CTD are labeled. Time points are labeled in the upper-right corner of each panel. (**A**) The IP$_6$ ligand is initially in bulk solvent. (**B**) Close-up view of the pore region in (A). (**C**) IP$_6$ enters the pore past the β-hairpin of CA, and an arginine side chain flips away from the R18 ring. (**D**) The R18 side chain coordinates IP$_6$. (**E**) IP$_6$ is coordinated to multiple R18 side chains. (**F**) IP$_6$ shifts toward the R18 ring. (**G**) IP$_6$ reorients in the binding pocket. (**H**) IP$_6$ is bound to the central arginine ring with R18 side chains contacting the negatively charged phosphates.
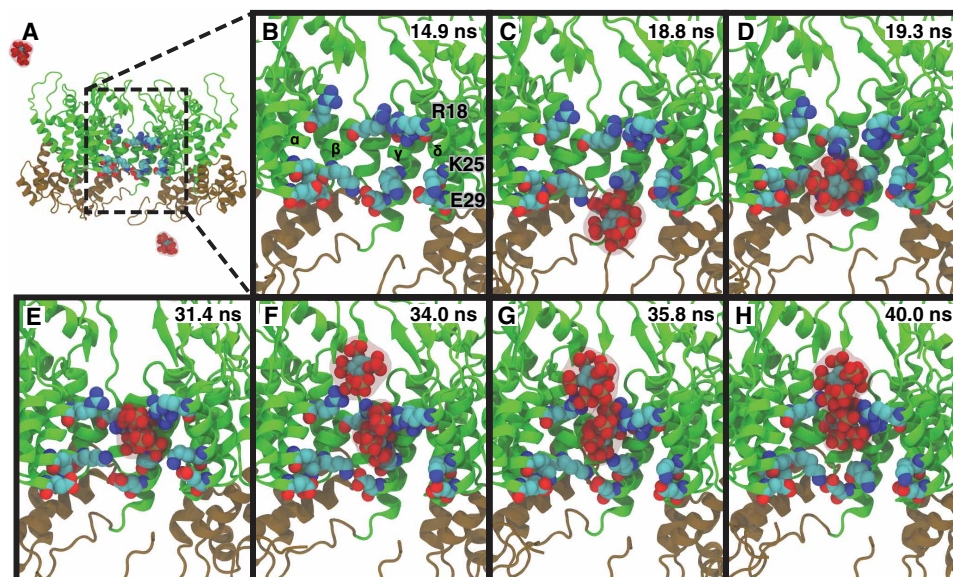

Fig. 3. Mechanism of IP$_6$ binding to CA hexamers. A series of snapshots from part of an MD trajectory show the chemical interactions involved in IP$_6$ binding to the CA hexamer. Four CA domains are shown in a side view of the hexamer, with helix H1 of the CA domain labeled as α, β, γ, and δ, respectively. Two additional CA domains (ε and ζ) are not shown for clarity. The R18 ring and residues (K25-E29) that form a salt-bridge interaction proximal to the CTD are labeled. Time points are labeled in the upper-right corner of each panel. (**A**) IP$_6$ molecules are initially in bulk solvent (two are shown). (**B**) Close-up view of the pore region in (A). (**C**) An IP$_6$ ligand enters the pore region from the CTD of CA. The K25-E29 salt-bridge interaction breaks, and K25 contacts IP$_6$. (**D**) A R18 side chain flips toward the CTD to coordinate IP$_6$. (**E**) IP$_6$ binds at the CTD side of the R18 ring. (**F**) A second IP$_6$ ligand enters the pore region, coordinated by an R18 side chain. (**G**) Multiple R18 side chains contact the second IP$_6$ ligand. (**H**) Two IP$_6$ molecules are bound to the R18 ring. Contacts between IP$_6$ and K25 are broken, and salt-bridge interactions between K25 and E29 reform.

involved more concerted motions in the CA NTDs compared to hexamers. The amounts of time ligands spent in bulk solvent before binding varied between CA hexamers and pentamers but were of similar time scale in the MD simulations.

Ligand density maps reveal alternate binding pockets

Transient metastable interactions between the protein and ligand can contribute substantially to the association process by lowering the energetics of intermediate states along the binding pathway.

Prior simulations of other systems have discovered a wide range of dynamical mechanisms used for binding, which do not involve direct interactions between the ligand and the binding site, including protein conformational changes that open up previously inaccessible binding pockets (19–21), the flipping of ligand configurations between several bound poses (15, 22), and metastable electrostatic interactions that guide ligands into the binding pocket (15, 16, 23–25). To assess the protein-ligand interactions that form during our simulations, we compute the spatial distribution occupied by the ligand's nonhydrogen atoms or, in other words, a 3D map of the ligand density (Fig. 4).

The ligand density maps reveal three sites of interaction between IP6 and the CA domain pentamer (Fig. 4, A and B). The primary binding site (site 1) has the highest density for the ligand and is positioned at the central pore of the pentamer, stabilized by interactions between IP6 and the R18 ring. Intriguingly, the simulations also showed a second lower-affinity binding site (site 2) at an intermolecular interface between the NTD of one CA domain and the CTD of the adjacent CA domain. At site 2 (fig. S2), IP6 binds between helices H3 and H4 of the CA NTD with several phosphate oxygen atoms forming contacts with the nitrogen atoms of N57, Q67, K70, and R173. Three of the four protein-ligand contacts (N57, Q67, and R173) have also been observed in prior x-ray structures of CA hexamers in complex with PF74, an HIV inhibitor (26). In addition, the CA residues that contribute to the protein-ligand interactions form a binding pocket that is structurally well preserved in atomic models of CA lattices [backbone root mean square deviation (RMSD) < 1.2 Å] derived from crystallography and cryo-EM

(6, 26, 27). This secondary site is the binding pocket for drug molecules that target the HIV capsid and inhibit viral replication including BI-2 (28), PF74, and GS-CA1 (29). Although the precise mechanisms of action for these compounds are currently unclear, several studies have suggested that small-molecule binding at this site may overly stabilize the capsid and perturb normal capsid disassembly processes, interfere with CA domain assembly processes that form intact capsids, or compete with nuclear import factor binding to the capsid, which is required for integration of the viral genome into the host cell (29–32).

Significant density is also observed at a third site (site 3) proximal to the CTD and consists of interactions between the flexible CA CTD tail and the negatively charged IP6 ligand. At site 3, IP6 phosphate oxygens form contacts with residues H226, K227, and R229 (fig. S2). There are no known drug molecules that currently bind to the CTD tail, which is a cleavage by-product of the retroviral aspartyl protease (e.g., HIV protease) during virion maturation. The aspartic acid moieties in the catalytic site of HIV protease may, in part, explain the affinity of the CTD tail for negatively charged molecules, although an alternative hypothesis is that the electrostatic properties of the CTD tail allow the CA CTD to form interactions with viral RNA that are necessary for recruiting and containing RNA in the mature capsid.

Ligand density maps for the CA domain hexamer are largely similar to that of the pentamer, containing the same sites and interactions with the IP6 ligand (Fig. 4, C and D). One noticeable difference, however, is that the primary site (site 1) in the hexamer is split into two continuous bodies corresponding to binding sites for IP6 above and below the R18 ring at high contour levels for the density ($\rho = 0.5$), whereas the map in the pentamer contains only a single density for site 1 above the R18 ring. This is consistent with our result that hexamers can bind two IP6 molecules, whereas pentamers bind only a single IP6 molecule. The ligand densities for sites 2 and 3 are not entirely either five- or sixfold symmetric around the pentamer or hexamer, respectively, owing to challenges in converging sampling statistics for IP6 and CA interactions at each of the binding sites. Overall, shape complementarity is noticeably higher for the IP6 molecule bound to the pentamer compared to the two bound to the hexamer at site 1 ($S_P = 603$ Å^2; $S_H = 417, 567$ Å^2) and for site 2 compared to site 3 ($S_2 = 696$ Å^2; $S_3 = 384$ Å^2; see also figs. S1 and S2). The binding sites discovered from the density analysis, however, agree well with known interactions at the CA domain, such as interactions with the capsid inhibitors (i.e., BI-2, PF74, and GS-CA1) and HIV protease. Our AA MD simulations did not contain prior information on these interactions, highlighting the potential of these simulations to detect novel binding sites for other molecules.

Free energy landscapes for IP6 binding

To quantify the energetics of the binding process, we computed the free energy landscape, i.e., the potential of mean force (PMF), for IP6 binding to CA hexamers and pentamers using umbrella sampling simulations, in which a 1D order parameter was used to describe the transport of IP6 to the R18 ring. The 1D order parameter, ξ, is defined as the projection of the displacement between the center of mass of the IP6 ligand and the center of mass of the backbone atoms of the R18 ring onto the vertical pore axis and is shown for the CA hexamer and CA pentamer (Fig. 5, A and B).

Both PMFs (Fig. 5, C and D) show that IP6 binding alleviates significant electrostatic repulsion between the R18 side chains and
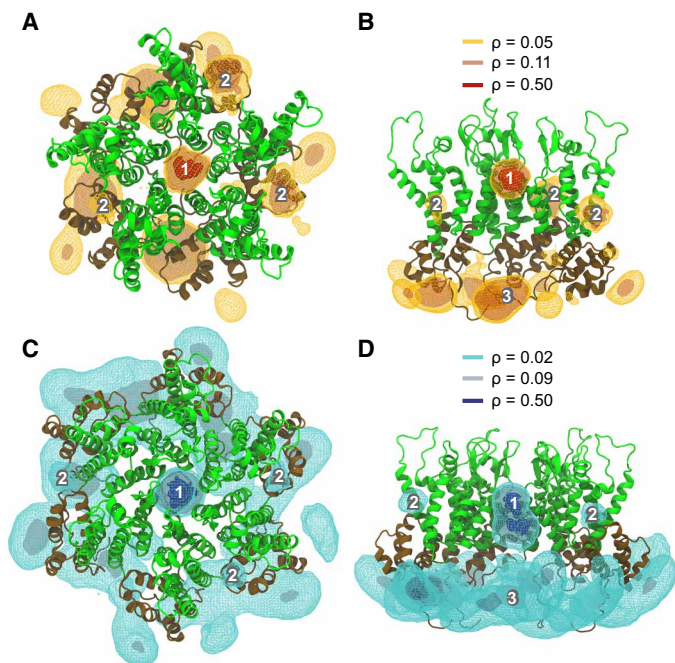

Fig. 4. Ligand density maps for IP6. The ligand densities are contoured at $\rho = 0.05$, 0.11, and 0.50 from orange to red, overlaid onto the structure of the CA pentamer, in a top-down view (**A**) and side view (**B**). Ligand densities are contoured at $\rho = 0.02$, 0.09, and 0.50 from light blue to dark blue, overlaid onto the structure of the CA hexamer in a top-down view (**C**) and side view (**D**). Densities contributing to interactions at sites 1, 2, and 3 are labeled in the figure, whereas densities proximal to the CA CTD (brown) form a third interaction site.
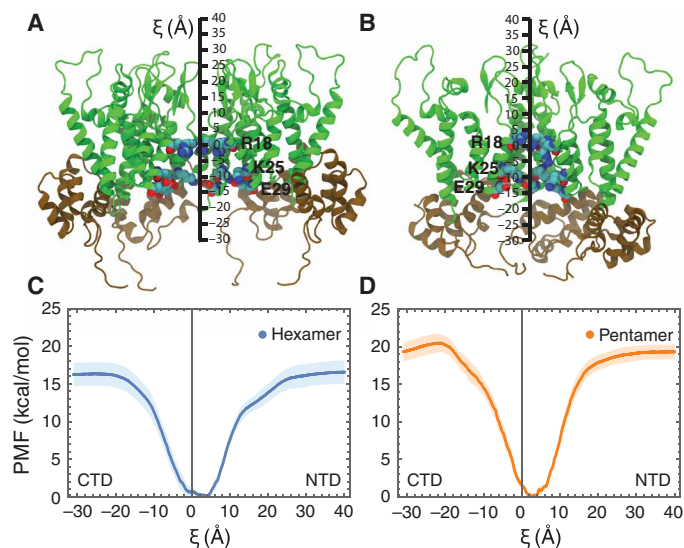
Fig. 5. The PMF for IP$_6$ binding. The order parameter, ξ, is used to describe IP$_6$ transport to the R18 ring. ξ is defined as the projection of the center-of-mass displacement between IP$_6$ and R18 residues onto the pore axis and is shown schematically for the CA hexamer (**A**) and the CA pentamer (**B**). The NTD is colored in green, whereas the CTD is colored in brown. Residues R18, K25, and K29 are labeled. (**C**) The 1D PMF for the CA hexamer is shown in blue. The shaded light blue regions denote the error in the PMF determined by block averaging. (**D**) The 1D PMF for the CA pentamer is plotted in orange. The shaded light-orange regions denote the error in the PMF determined by block averaging. The pore axis is oriented such that positive values correspond to the CA NTD, whereas negative values correspond to the CA CTD.

contain deep free energy minima proximal to the R18 ring ($\xi = 0$ Å). The hexamer PMF has a broad free energy basin, reflecting a larger pore volume for IP$_6$ diffusion, and a global free energy minimum positioned at $\xi = 3.7$ Å. There is a second local minimum in the hexamer PMF at $\xi = -0.8$ Å corresponding to the binding site below the R18 ring, which is slightly less stable relative to the global free energy minimum ($\Delta G = 0.6$ kcal/mol). This is consistent with electron density maps derived from x-ray crystal structures of CA hexamers in complex with IP$_6$ that revealed stronger densities for binding sites above the ring than below the ring (*9*, *10*). In contrast, the pentamer PMF has a narrower free energy basin owing to a more restricted and compact helix H1 region below the R18 ring in the CA pentamer as compared to that of the CA hexamer and has a single overall free energy minimum located at $\xi = 2.7$ Å. Ligand entry from the CTD side of the pentamer is unfavorable compared to entry from the NTD region, and conformational states in which IP$_6$ is below the R18 ring ($\xi < 0$ Å) are destabilized ($\Delta G > 1.6$ kcal/mol). In both hexamer and pentamer PMFs, the CA domain β-hairpin ($\xi \sim 5$ to 15 Å) did not form high free energy barriers to ligand entry.

As the ligand exits into bulk solvent ($\xi > 25$ Å and $\xi < -20$ Å), both PMFs plateau to a constant value as expected, because the protein and ligand no longer interact. Positive values for the order parameter, ξ, correspond to the binding pathway energetics of IP$_6$ entering the pore from the exterior of the mature capsid (NTD), whereas negative values of ξ correspond to the energetics of IP$_6$ entering the pore from the interior of the mature capsid (CTD). The total free energy difference of transporting IP$_6$ to the R18 ring is greater in the pentamer ($\Delta G = 19.3$ kcal/mol) than in the hexamer ($\Delta G = 16.4$ kcal/mol), indicating that IP$_6$ binding stabilizes CA pen-

tamers more than CA hexamers in the fullerene shell. The calculated binding free energies are consistent with that of four to six Arg-phosphate interactions, which have higher stabilities (*33*–*35*) than that of Arg-Glu interactions [$\Delta G_{RE} = \sim 4$ to 5 kcal/mol for a single pair (*36*, *37*)]. Hexamer configurations can form an additional Arg-phosphate interaction compared to pentamer configurations; however, the smaller pentamer pore facilitates closer coordination of IP$_6$ phosphate groups by R18 side chains. Free volume corrections to account for finite-size effects also lower the effective equilibrium dissociation constants derived from the PMFs by approximately 4 kcal/mol (*38*). Negative-stained electron microscopy studies demonstrated that removal of the charged arginine ring by an R18A mutation forms CA assemblies with spherical, fullerene, and spiral structures, hypothesized to occur from an increased frequency of pentamer incorporation into the CA hexagonal lattice (*5*, *39*). Although the R18A mutation removes the primary site of CA interaction with IP$_6$, the mutation also reduces electrostatic repulsion between CA subunits at R18, analogous to the effect of IP$_6$ binding. Overall, our findings suggest that IP$_6$ preferentially binds to and stabilizes CA pentamers over CA hexamers as a result of the more compact and closely packed H1 pore helices in the pentamer and a subsequent greater electrostatic repulsion at the R18 ring. Given the higher number of hexamers in the capsid lattice, a large amount of IP$_6$ in total should be found among the hexamers.

DISCUSSION

Collectively, our results suggest that CA hexamer and pentamer building blocks of the fullerene capsid bind IP$_6$ with rather different binding modes. At high IP$_6$ concentrations (i.e., [IP$_6$]:[CA] = 1:3), hexamers can bind IP$_6$ at a secondary site below the R18 ring, whereas at low IP$_6$ concentrations ([IP$_6$]:[CA] = 1:6), IP$_6$ alternates between the two binding sites, although the site above the R18 ring is lower in free energy ($\Delta G = -0.6$ kcal/mol). Experimental estimates using radiolabeled IP$_6$ ligands suggest that ~300 IP$_6$ molecules are packaged per viral particle, which contains ~1500 CA domains, indicating that the latter case is more likely to occur (*7*). The molecular pathways by which IP$_6$ binds involve a conformational twist in the pentamers, which may also be aided by the inclusion of pentamers at highly curved regions of the capsid surface. Binding below the R18 ring in pentamers is less favorable because pentamers have a compact and tighter pore relative to that of hexamers. Ligand density calculations show that interactions at the R18 ring are consistent with the differential binding modes and reveal two additional sites of IP$_6$ interaction, one of which is a previously known capsid inhibitor binding pocket (site 2) and the other consists of an interaction between the CTD tail and negatively charged molecules that could reflect capsid and RNA interactions (site 3). The two weaker affinity sites are metastable, and similar sites found in AA MD simulations of other systems have been reported to form higher-affinity binding sites for different ligands (*22*, *40*). Radiolabeled ligand binding and mutagenesis experiments could further investigate protein-ligand interactions at these sites.

The computed PMFs demonstrate that IP$_6$ binding stabilizes individual pentamers more than individual hexamers. Since CA spontaneously assembles into both helical tubes and fullerene cones in vitro (*41*), and pentameric "defects" (*5*, *6*, *42*) are required to produce fullerene cones but are not present in helical tubes, this result indicates that the binding of IP$_6$ shifts the equilibrium population of

hexamers and pentamers toward increased pentamer formation, thereby promoting the fullerene mode of assembly. It is of note to recognize that the pathways discussed characterize the binding of IP_6 to preformed mature capsid complexes and not the molecular pathways for the co-assembly of CA and IP_6, which may differ. Further simulations that target the co-assembly of CA and IP_6 will likely require coarse-grained molecular simulation techniques to overcome the long time scale barriers associated with biomolecular assembly phenomena (43, 44). The computed thermodynamic quantities, however, are state functions that do not change in response to the particular path taken, so the IP_6 interactions revealed by the ligand density maps are therefore general. Experimental strategies using engineered disulfide cross-links to stabilize hexamer or pentamer constructs (39, 45) combined with binding assays may also uncover additional thermodynamic quantities relevant to IP_6 binding, and AA simulations of large-scale CA lattices bound to IP_6 could reveal how IP_6 affects global structural properties, such as lattice flexibility.

Since inositol phosphates play important physiological roles in promoting and stabilizing the assembly of the HIV-1 capsid, could the removal of IP_6 be involved in disassembly processes? One possible mechanism is that acidic conditions simultaneously trigger protonation of IP_6 phosphate groups and H12, thus reducing the affinity of IP_6 for the R18 ring and opening of the capsid pores. Although pH has been known to trigger the release of genetic material in viruses by acidification of endosomal vesicles during intracellular transport (46), it is unclear whether HIV capsids are exposed to similarly low pH conditions during infection in either endocytic or membrane fusion pathways (47). In addition, IP_6 can chelate divalent metal cations, and a potential mechanism for nucleotide entry into capsid pores blocked by IP_6 is for free nucleotides to transfer associated divalent cations to IP_6 to unblock the pore.

In this work, we have elucidated the molecular mechanisms responsible for the stabilization of mature capsids by IP_6 through extensive AA MD simulations. Additional investigations can further probe how retroviruses exploit environmental cues to initiate replication processes.

MATERIALS AND METHODS
AA models for the CA hexamer, pentamer, and IP_6
The initial atomic models for the CA hexamer and pentamer were constructed from the x-ray crystal structures for the CA hexamer in the closed and open conformations (PDB ID: 3H47 and 5HGL, respectively) and the cryo-EM structure for the CA pentamer in the closed conformation (PDB ID: 5MCY). A homology model for the open CA pentamer was constructed on the basis of aligning individual CA domains and transplanting the β-hairpin gate (residues 1 to 16) from the open CA hexamer onto the closed pentamer. Missing amino acid residue backbones were built using MODELLER (48), and missing side chains were built using SCWRL4 (49). The hexamer and pentamer systems, which contained a total of 287,048 and 286,715 atoms, respectively, were solvated and neutralized by adding Na^+ and Cl^- ions to the bulk solution until the salt concentration was 150 mM NaCl. Periodic boundary conditions were imposed on an orthorhombic unit cell of approximately 141 Å × 141 Å × 141 Å for both the hexameric and pentameric systems. The AA potential energy function CHARMM36m (50, 51) for proteins and the TIP3P (52) potential energy function for water were used. Electrostatic interactions were computed using the particle mesh Ewald algo-

rithm, and short-range, nonbonded interactions were truncated to 12 Å. Harmonic restraints were applied to the center of masses of two groups of residues (residues 179 to 189 and residues 200 to 207) in α-helices, H9 and H10, at the CTD interface between distinct hexamer and pentamer subunits to maintain the relative position of the CTD interface derived from an atomic model of the complete HIV-1 capsid (6). The relative center-of-mass positions for the two groups of residues were computed after RMSD-aligning individual CA hexamers and pentamers of the capsid and used as the equilibrium positions for the harmonic restraints to mimic the average curvature in the capsid, along with a light force constant of $k = 0.5$ kcal/mol. The solvated system was energy minimized and equilibrated under constant pressure and temperature (NPT) conditions at 1 atm and 310 K with a 2-fs time step. Minimization and equilibration procedures were performed using the AA MD simulation package NAMD 2.13 (53).

MD simulations for IP_6 binding
IP_6 molecules were initially placed at random positions and orientations in bulk solvent, approximately 10 Å away from any nonwater molecules. Fifteen IP_6 molecules were used to increase sampling times. The IP_6 was parameterized using the CHARMM General Force Field (CGenFF) (54). For each CA domain system, the histidine residues, H12, were completely protonated or deprotonated. Salt concentration was adjusted for the ligand charge to maintain 150 mM NaCl and an electrostatically neutral system. After a 50-ns equilibration run, eight systems consisting of hexamer/pentamer, open/closed, and H12 protonated/deprotonated combinations were prepared for simulation on Anton 2 at the Pittsburgh Supercomputing Center (14). For all production simulations, bond lengths for hydrogen atoms were constrained using the M-SHAKE algorithm (55). An r-RESPA integrator was used with a time step of 2 fs (56); long-range electrostatics were computed every 6 fs. Long-range electrostatics were calculated using the k-space Gaussian split Ewald method (57). Short-range interactions, including van der Waals and short-range electrostatics, were truncated at 9 Å. Simulations in the constant NPT ensemble were performed using a chained Nosé-Hoover thermostat at 310 K and isotropic Martyna-Tobias-Klein barostat at 1 atm (58). Each trajectory (four CA hexamers and four CA pentamers) was simulated until no additional binding events were observed. In aggregate, total simulation time was 47 μs for the CA hexamer and pentamer systems (see table S1).

Ligand density calculations
The trajectories from production-level simulations were subsampled at 0.12-ns intervals and aggregated into pentamer or hexamer systems. For each frame, the atomic system was aligned by minimizing the RMSD of the protein backbone atoms with respect to the crystallographic structure. Cartesian coordinates for the nonhydrogen atoms of IP_6 were recorded, and the density of atomic positions $\rho(\vec{r})$ was calculated, using a hard-sphere van der Walls approximation on a discretized grid with a spacing of 0.5 Å × 0.5 Å × 0.5 Å. The 3D ligand density map was subsequently contoured at $\rho = 0.05, 0.11$, and 0.50 for the CA pentamer systems and $\rho = 0.02, 0.09$, and 0.05 for the CA hexamer systems.

Umbrella sampling
The free energy landscape (PMF) of IP_6 binding was computed using an umbrella sampling strategy (59). All systems contained a

single IP$_6$ molecule, either a CA hexamer or pentamer in the open conformation, and a protonated H12 residue. A 1D order parameter, ξ, is used to describe the relative distance to the R18 ring. ξ specifies the projection of the displacement vector between the center of mass of the IP$_6$ ligand ($\vec{r}$) and center of mass of the backbone atoms of the R18 ring ($\vec{r}_{R18}$) onto the z axis [e.g., $\xi = (\vec{r} - \vec{r}_{R18}) \cdot \hat{z}$]. The umbrella sampling windows consisted of CA domain complexes and the IP$_6$ ligand positioned in 0.2-Å increments along ξ. The initial coordinates were obtained using targeted MD simulations in NAMD, using the solvated CA hexamer or pentamer systems. Three hundred sixty umbrella sampling windows were used to compute the PMFs. Harmonic biasing potentials with a force constant of 20 kcal/mol per Å^2 centered on ξ were used. All other restraints and interactions were computed as described during the equilibration phase. The total simulation time for the CA hexamer is 28.8 µs. The total simulation for the CA pentamer is 28.8 µs. Each PMF, $W(\xi)$, was computed using the weighted histogram analysis method (WHAM) to unbias and recombine the sampled distribution functions from all windows (60, 61). The statistical uncertainty in each PMF was evaluated using the approach of block averaging (62). For each PMF, the time series was divided into five blocks, and WHAM was used to calculate a PMF from the data in each block. The standard deviation of the five PMFs was reported. Using 5 to 15 blocks, all gave qualitatively similar results.

SUPPLEMENTARY MATERIALS

Supplementary material for this article is available at http://advances.sciencemag.org/cgi/content/full/6/38/eabc6465/DC1

View/request a protocol for this paper from *Bio-protocol*.

REFERENCES AND NOTES

1. E. O. Freed, HIV-1 assembly, release and maturation. *Nat. Rev. Microbiol.* **13**, 484–496 (2015).
2. E. M. Campbell, T. J. Hope, HIV-1 capsid: The multifaceted key player in HIV-1 infection. *Nat. Rev. Microbiol.* **13**, 471–483 (2015).
3. F. K. M. Schur, W. J. H. Hagen, M. Rumlová, T. Ruml, B. Müller, H.-G. Kräusslich, J. A. G. Briggs, Structure of the immature HIV-1 capsid in intact virus particles at 8.8 Å resolution. *Nature* **517**, 505–508 (2015).
4. B. K. Ganser, S. Li, V. Y. Klishko, J. T. Finch, W. I. Sundquist, Assembly and analysis of conical models for the HIV-1 core. *Science* **283**, 80–83 (1999).
5. B. K. Ganser-Pornillos, U. K. von Schwedler, K. M. Stray, C. Aiken, W. I. Sundquist, Assembly properties of the human immunodeficiency virus type 1 CA protein. *J. Virol.* **78**, 2545–2552 (2004).
6. S. Mattei, B. Glass, W. J. H. Hagen, H.-G. Kräusslich, J. A. G. Briggs, The structure and flexibility of conical HIV-1 capsids determined within intact virions. *Science* **354**, 1434–1437 (2016).
7. D. A. Jacques, W. A. McEwan, L. Hilditch, A. J. Price, G. J. Towers, L. C. James, HIV-1 uses dynamic capsid pores to import nucleotides and fuel encapsidated DNA synthesis. *Nature* **536**, 349–353 (2016).
8. R. A. Dick, D. L. Mallery, V. M. Vogt, L. C. James, IP6 regulation of HIV capsid assembly, stability, and uncoating. *Viruses* **10**, 640 (2018).
9. D. L. Mallery, C. L. Márquez, W. A. McEwan, C. F. Dickson, D. A. Jacques, M. Anandapadamanaban, K. Bichel, G. J. Towers, A. Saiardi, T. Böcking, L. C. James, IP6 is an HIV pocket factor that prevents capsid collapse and promotes DNA synthesis. *eLife* **7**, e35335 (2018).
10. R. A. Dick, K. K. Zadrozny, C. Xu, F. K. M. Schur, T. D. Lyddon, C. L. Ricana, J. M. Wagner, J. R. Perilla, B. K. Ganser-Pornillos, M. C. Johnson, O. Pornillos, V. M. Vogt, Inositol phosphates are assembly co-factors for HIV-1. *Nature* **560**, 509–512 (2018).
11. D. L. Mallery, K. M. R. Faysal, A. Kleinpeter, M. S. C. Wilson, M. Vaysburd, A. J. Fletcher, M. Novikova, T. Böcking, E. O. Freed, A. Saiardi, L. C. James, Cellular IP6 levels limit HIV production while viruses that cannot efficiently package IP6 are attenuated for infection and replication. *Cell Rep.* **29**, 3983–3996.e4 (2019).
12. B. K. Ganser-Pornillos, A. Cheng, M. Yeager, Structure of full-length HIV-1 CA: A model for the mature capsid lattice. *Cell* **131**, 70–79 (2007).
13. J. R. Perilla, K. Schulten, Physical properties of the HIV-1 capsid from all-atom molecular dynamics simulations. *Nat. Commun.* **8**, 15959 (2017).
14. D. E. Shaw, J. P. Grossman, J. A. Bank, B. Batson, J. A. Butts, J. C. Chao, M. M. Deneroff, R. O. Dror, A. Even, C. H. Fenton, A. Forte, J. Gagliardo, G. Gill, B. Greskamp, C. R. Ho, D. J. Ierardi, L. Iserovich, J. S. Kuskin, R. H. Larson, T. Layman, L.-S. Lee, A. K. Lerer, C. Li, D. Killebrew, K. M. Mackenzie, S. Y.-H. Mok, M. A. Moraes, R. Mueller, L. J. Nociolo, J. L. Peticolas, T. Quan, D. Ramot, J. K. Salmon, D. P. Scarpazza, U. B. Schafer, N. Siddique, C. W. Snyder, J. Spengler, P. T. P. Tang, M. Theobald, H. Toma, B. Towles, B. Vitale, S. C. Wang, C. Young, in *SC '14: Proceedings of the International Conference for High Performance Computing, Networking, Storage and Analysis* (IEEE, 2014), pp. 41–53.
15. A. Yu, H. Salazar, A. J. R. Plested, A. Y. Lau, Neurotransmitter funneling optimizes glutamate receptor kinetics. *Neuron* **97**, 139–149.e4 (2018).
16. A. Yu, A. Y. Lau, Glutamate and glycine binding to the NMDA receptor. *Structure* **26**, 1035–1043.e2 (2018).
17. M. Obr, H.-G. Kräusslich, The secrets of the stability of the HIV-1 capsid. *eLife* **7**, e38895 (2018).
18. P. Craveur, A. T. Gres, K. A. Kirby, D. Liu, J. A. Hammond, Y. Deng, S. Forli, D. S. Goodsell, J. R. Williamson, S. G. Sarafianos, A. J. Olson, Novel intersubunit interaction critical for HIV-1 core assembly defines a potentially targetable inhibitor binding pocket. *MBio* **10**, e02858-18 (2019).
19. H. A. Carlson, J. A. McCammon, Accommodating protein flexibility in computational drug design. *Mol. Pharmacol.* **57**, 213–218 (2000).
20. J. R. Schames, R. H. Henchman, J. S. Siegel, C. A. Sotriffer, H. Ni, J. A. McCammon, Discovery of a novel binding trench in HIV integrase. *J. Med. Chem.* **47**, 1879–1881 (2004).
21. Y. Shan, E. T. Kim, M. P. Eastwood, R. O. Dror, M. A. Seeliger, D. E. Shaw, How does a drug molecule find its target binding site? *J. Am. Chem. Soc.* **133**, 9181–9183 (2011).
22. R. O. Dror, A. C. Pan, D. H. Arlow, D. W. Borhani, P. Maragakis, Y. Shan, H. Xu, D. E. Shaw, Pathway and mechanism of drug binding to G-protein-coupled receptors. *Proc. Natl. Acad. Sci. U.S.A.* **108**, 13118–13123 (2011).
23. R. C. Tan, T. N. Truong, J. A. McCammon, J. L. Sussman, Acetylcholinesterase: Electrostatic steering increases the rate of ligand binding. *Biochemistry* **32**, 401–403 (1993).
24. A. Yu, R. Alberstein, A. Thomas, A. Zimmet, R. Grey, M. L. Mayer, A. Y. Lau, Molecular lock regulates binding of glycine to a primitive NMDA receptor. *Proc. Natl. Acad. Sci. U.S.A.* **113**, E6786–E6795 (2016).
25. A. Yu, A. Y. Lau, Energetics of glutamate binding to an ionotropic glutamate receptor. *J. Phys. Chem. B* **121**, 10436–10442 (2017).
26. A. Bhattacharya, S. L. Alam, T. Fricke, K. Zadrozny, J. Sedzicki, A. B. Taylor, B. Demeler, O. Pornillos, B. K. Ganser-Pornillos, F. Diaz-Griffero, D. N. Ivanov, M. Yeager, Structural basis of HIV-1 capsid recognition by PF74 and CPSF6. *Proc. Natl. Acad. Sci. U.S.A.* **111**, 18625–18630 (2014).
27. G. Zhao, J. R. Perilla, E. L. Yufenyuy, X. Meng, B. Chen, J. Ning, J. Ahn, A. M. Gronenborn, K. Schulten, C. Aiken, P. Zhang, Mature HIV-1 capsid structure by cryo-electron microscopy and all-atom molecular dynamics. *Nature* **497**, 643–646 (2013).
28. L. Lamorte, S. Titolo, C. T. Lemke, N. Goudreau, J.-F. Mercier, E. Wardrop, V. B. Shah, U. K. von Schwedler, C. Langelier, S. S. R. Banik, C. Aiken, W. I. Sundquist, S. W. Mason, Discovery of novel small-molecule HIV-1 replication inhibitors that stabilize capsid complexes. *Antimicrob. Agents Chemother.* **57**, 4622–4631 (2013).
29. K. Singh, F. Gallazzi, K. J. Hill, D. H. Burke, M. J. Lange, T. P. Quinn, U. Neogi, A. Sönnerborg, GS-CA compounds: First-in-class HIV-1 capsid inhibitors covering multiple grounds. *Front. Microbiol.* **10**, 1227 (2019).
30. S. Thenin-Houssier, S. T. Valente, HIV-1 capsid inhibitors as antiretroviral agents. *Curr. HIV Res.* **14**, 270–282 (2016).
31. S. R. Yant, A. Mulato, D. Hansen, W. C. Tse, A. Niedziela-Majka, J. R. Zhang, G. J. Stepan, D. Jin, M. H. Wong, J. M. Perreira, E. Singer, G. A. Papalia, E. Y. Hu, J. Zheng, B. Lu, S. D. Schroeder, K. Chou, S. Ahmadyar, A. Liclican, H. Yu, N. Novikov, E. Paoli, D. Gonik, R. R. Ram, M. Hung, W. M. McDougall, A. L. Brass, W. I. Sundquist, T. Cihlar, J. O. Link, A highly potent long-acting small-molecule HIV-1 capsid inhibitor with efficacy in a humanized mouse model. *Nat. Med.* **25**, 1377–1384 (2019).
32. S. K. Carnes, J. H. Sheehan, C. Aiken, Inhibitors of the HIV-1 capsid, a target of opportunity. *Curr. Opin. HIV AIDS* **13**, 359–365 (2018).
33. D. J. Mandell, I. Chorny, E. S. Groban, S. E. Wong, E. Levine, C. S. Rapp, M. P. Jacobson, Strengths of hydrogen bonds involving phosphorylated amino acid side chains. *J. Am. Chem. Soc.* **129**, 820–827 (2007).
34. T. Hunter, Why nature chose phosphate to modify proteins. *Philos. Trans. R. Soc. Lond. Ser. B Biol. Sci.* **367**, 2513–2516 (2012).
35. A. S. Woods, S. Ferré, Amazing stability of the arginine–phosphate electrostatic interaction. *J. Proteome Res.* **4**, 1397–1402 (2005).
36. A. Masunov, T. Lazaridis, Potentials of mean force between ionizable amino acid side chains in water. *J. Am. Chem. Soc.* **125**, 1722–1730 (2003).
37. X. Rozanska, C. Chipot, Modeling ion–ion interaction in proteins: A molecular dynamics free energy calculation of the guanidinium-acetate association. *J. Chem. Phys.* **112**, 9691–9694 (2000).

38. J. Chen, C. L. Brooks, H. A. Scheraga, Revisiting the carboxylic acid dimers in aqueous solution: Interplay of hydrogen bonding, hydrophobic interactions, and entropy. *J. Phys. Chem. B* **112**, 242–249 (2008).

39. O. Pornillos, B. K. Ganser-Pornillos, M. Yeager, Atomic-level modelling of the HIV capsid. *Nature* **469**, 424–427 (2011).

40. R. O. Dror, H. F. Green, C. Valant, D. W. Borhani, J. R. Valcourt, A. C. Pan, D. H. Arlow, M. Canals, J. R. Lane, R. Rahmani, J. B. Baell, P. M. Sexton, A. Christopoulos, D. E. Shaw, Structural basis for modulation of a G-protein-coupled receptor by allosteric drugs. *Nature* **503**, 295–299 (2013).

41. S. Li, C. P. Hill, W. I. Sundquist, J. T. Finch, Image reconstructions of helical assemblies of the HIV-1 CA protein. *Nature* **407**, 409–413 (2000).

42. D. L. Bush, V. M. Vogt, In vitro assembly of retroviruses. *Annu. Rev. Virol.* **1**, 561–580 (2014).

43. J. M. A. Grime, J. F. Dama, B. K. Ganser-Pornillos, C. L. Woodward, G. J. Jensen, M. Yeager, G. A. Voth, Coarse-grained simulation reveals key features of HIV-1 capsid self-assembly. *Nat. Commun.* **7**, 11568 (2016).

44. A. Yu, K. A. Skorupka, A. J. Pak, B. K. Ganser-Pornillos, O. Pornillos, G. A. Voth, TRIM5α self-assembly and compartmentalization of the HIV-1 viral capsid. *Nat. Commun.* **11**, 1307 (2020).

45. O. Pornillos, B. K. Ganser-Pornillos, S. Banumathi, Y. Hua, M. Yeager, Disulfide bond stabilization of the hexameric capsomer of human immunodeficiency virus. *J. Mol. Biol.* **401**, 985–995 (2010).

46. M. Marsh, A. Helenius, Virus entry: Open sesame. *Cell* **124**, 729–740 (2006).

47. K. Miyauchi, Y. Kim, O. Latinovic, V. Morozov, G. B. Melikyan, HIV enters cells via endocytosis and dynamin-dependent fusion with endosomes. *Cell* **137**, 433–444 (2009).

48. B. Webb, A. Sali, Comparative protein structure modeling using MODELLER. *Curr. Protoc. Bioinformatics* **56**, 5.6.1–5.6.37 (2016).

49. G. G. Krivov, M. V. Shapovalov, R. L. Dunbrack Jr., Improved prediction of protein side-chain conformations with SCWRL4. *Proteins* **77**, 778–795 (2009).

50. A. D. MacKerell, D. Bashford, M. Bellott, R. L. Dunbrack, J. D. Evanseck, M. J. Field, S. Fischer, J. Gao, H. Guo, S. Ha, D. Joseph-McCarthy, L. Kuchnir, K. Kuczera, F. T. K. Lau, C. Mattos, S. Michnick, T. Ngo, D. T. Nguyen, B. Prodhom, W. E. Reiher, B. Roux, M. Schlenkrich, J. C. Smith, R. Stote, J. Straub, M. Watanabe, J. Wiórkiewicz-Kuczera, D. Yin, M. Karplus, All-atom empirical potential for molecular modeling and dynamics studies of proteins. *J. Phys. Chem. B* **102**, 3586–3616 (1998).

51. J. Huang, S. Rauscher, G. Nawrocki, T. Ran, M. Feig, B. L. de Groot, H. Grubmüller, A. D. MacKerell Jr., CHARMM36m: An improved force field for folded and intrinsically disordered proteins. *Nat. Methods* **14**, 71–73 (2017).

52. W. L. Jorgensen, J. Chandrasekhar, J. D. Madura, R. W. Impey, M. L. Klein, Comparison of simple potential functions for simulating liquid water. *J. Chem. Phys.* **79**, 926–935 (1983).

53. J. C. Phillips, R. Braun, W. Wang, J. Gumbart, E. Tajkhorshid, E. Villa, C. Chipot, R. D. Skeel, L. Kalé, K. Schulten, Scalable molecular dynamics with NAMD. *J. Comput. Chem.* **26**, 1781–1802 (2005).

54. K. Vanommeslaeghe, E. Hatcher, C. Acharya, S. Kundu, S. Zhong, J. Shim, E. Darian, O. Guvench, P. Lopes, I. Vorobyov, A. D. Mackerell Jr., CHARMM general force field: A force field for drug-like molecules compatible with the CHARMM all-atom additive biological force fields. *J. Comput. Chem.* **31**, 671–690 (2010).

55. V. Kräutler, W. F. van Gunsteren, P. H. Hünenberger, A fast SHAKE algorithm to solve distance constraint equations for small molecules in molecular dynamics simulations. *J. Comput. Chem.* **22**, 501–508 (2001).

56. M. Tuckerman, B. J. Berne, G. J. Martyna, Reversible multiple time scale molecular dynamics. *J. Chem. Phys.* **97**, 1990–2001 (1992).

57. Y. Shan, J. L. Klepeis, M. P. Eastwood, R. O. Dror, D. E. Shaw, Gaussian split Ewald: A fast Ewald mesh method for molecular simulation. *J. Chem. Phys.* **122**, 054101 (2005).

58. G. J. Martyna, D. J. Tobias, M. L. Klein, Constant pressure molecular dynamics algorithms. *J. Chem. Phys.* **101**, 4177–4189 (1994).

59. A. Yu, T. Wied, J. Belcher, A. Y. Lau, in *Ionotropic Glutamate Receptor Technologies* (Humana Press, 2016), pp. 119–132; https://doi.org/10.1007/978-1-4939-2812-5_9.

60. S. Kumar, J. M. Rosenberg, D. Bouzida, R. H. Swendsen, P. A. Kollman, THE weighted histogram analysis method for free-energy calculations on biomolecules. I. The method. *J. Comput. Chem.* **13**, 1011–1021 (1992).

61. M. Souaille, B. Roux, Extension to the weighted histogram analysis method: Combining umbrella sampling with free energy calculations. *Comput. Phys. Commun.* **135**, 40–57 (2001).

62. F. Zhu, G. Hummer, Convergence and error estimation in free energy calculations using the weighted histogram analysis method. *J. Comput. Chem.* **33**, 453–465 (2012).

Citation: A. Yu, E. M. Y. Lee, J. Jin, G. A. Voth, Atomic-scale characterization of mature HIV-1 capsid stabilization by inositol hexakisphosphate (IP₆). *Sci. Adv.* **6**, eabc6465 (2020).